Homogeneous and heterogeneous deformation mechanisms in an austenitic polycrystalline Ti–50.8 at.% Ni thin tube under tension. Investigation via temperature and strain fields measurements

D. Favier [a,*], H. Louche [b], P. Schlosser [a], L. Orgéas [a], P. Vacher [b], L. Debove [a]

[a] *Laboratoire Sols-Solides-Structures (3S), CNRS – Universités de Grenoble (INPG-UJF), BP 53, 38041 Grenoble Cedex 9, France*
[b] *Symme, Polytech'Savoie, BP 80043, 74944 Annecy Le Vieux Cedex, France*

Abstract

An initially austenitic polycrystalline Ti–50.8 at.% Ni thin-walled tube with small grain sizes has been deformed under tension in air at ambient temperature and moderate nominal axial strain rate. Temperature and strain fields were measured using visible-light and infrared digital cameras. In a first apparently elastic deformation stage, both strain and temperature fields are homogeneous and increase in tandem. This stage is followed by initiation, propagation and growth of localized helical bands inside which strain and temperature increases are markedly higher than in the surrounding regions. During the first apparently elastic stage of the unloading, both strain and temperature fields are homogeneous and decrease. The temperature and strain fields evolutions are then analysed in order to determine the deformation mechanisms (types and extents of phase transformations, variants (de)twinning, macroscopic banding) involved during the homogeneous and heterogeneous stages of deformation throughout the whole tube. The findings have significant implications for the understanding and modelling of superelastic behaviour of NiTi shape memory alloys.
© 2007 Acta Materialia Inc. Published by Elsevier Ltd. All rights reserved.

Keywords: NiTi shape memory alloys; Tension test; Localisation; Phase transformations; Strain and temperature fields

1. Introduction

Shape memory alloys (SMAs) are now employed in a large number of applications in the fields of aeronautical, biomedical and structural engineering. Owing to their outstanding superelastic behaviour at human body temperature and to their biocompatibility, polycrystalline Ti–50.8 at.% Ni SMAs are being increasingly used for biomedical applications (e.g., human implants and surgical instruments).

The applications based on the peculiar properties of these NiTi SMAs are increasingly being designed using numerical simulation and finite element softwares in which three-dimensional constitutive equations are implemented to model the thermomechanical behaviour of these alloys. These constitutive equations are mostly based on the conventional understanding of the superelastic tensile engineering strain–stress curve shown in Fig. 1. Initially, the material is in austenite phase (A) since the testing temperature is above Af. Af is the temperature at which the martensite phase (M), which is stable at low temperature, is completely transformed by heating to the austenite phase A, which is stable at high temperature. The loading curve of Fig. 1 is usually divided in a first linear part (1) associated with the elastic deformation of A, a second one (2) associated with the A–M transformation occurring along an upper stress plateau (for NiTi SMAs) and then a third one (3) associated with the elastic deformation of oriented martensite variants. When the load is progressively removed, the reverse M–A transformation occurs along a lower stress plateau (5) after an initial linear stage (4)
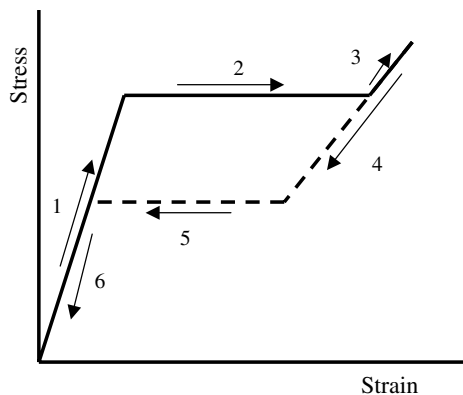
Fig. 1. Oversimplified superelastic strain–stress curve. Conventional understanding: (1) Elastic deformation of austenite. (2) Austenite to oriented martensite transformation. (3) and (4) Elastic deformation of oriented martensite. (5) Oriented martensite to austenite reverse transformation. (6) Elastic deformation of austenite.

associated with the elastic unloading of the oriented martensite M. The complete reverse transformation is followed by the elastic unloading of A during stage (6). Model of the superelastic behaviour of NiTi SMAs based on this above simple analysis is a preliminary step. However, a better understanding of the complex phenomena occurring during all these stages is necessary to improve this modelling.

Intensive experimental investigations have been carried out in recent decades to characterize and understand deformation mechanisms associated with the superelasticity of SMAs. Most of these studies have been achieved in tension using wires, strips or bone-shaped samples. It is now well established that uniaxial tensile superelastic deformation of polycrystalline NiTi SMAs often exhibits localized Lüders-like deformation modes [1–9], which occur during the upper (2) and lower (5) plateaux sketched in Fig. 1. This heterogeneous deformation may disappear for other mechanical loadings such as compression or shear [5] or tension–torsion combined tests [6], and can also be observed during the ferroelastic tensile deformation of polycrystalline NiTi SMAs [10]. The localization has been studied using qualitative optical observations [1,3,6–8], multiple extensometers [2,4,5] and full-field temperature measurements [3,9]. In comparison, the other stages (1), (3), (4) and (6) have less been studied. However, Brinson et al. [7] presented some results that showed clearly the occurrence of several deformation mechanisms other than elastic distortion of the crystalline structure during each of these stages.

The references cited above and numerous other works have raised important issues in the fundamental understanding and modelling of stress-induced phase transformation in polycrystalline NiTi SMAs. For optimal implementation of NiTi SMAs in engineering applications a thorough understanding of the material behaviour is necessary. Therefore, the present contribution reports and analyses results concerning a tensile test on a NiTi polycrystalline thin-walled tube during which thermal as well

as kinematical full-field measurements have been simultaneously carried out.

The material properties and experimental procedures are described in Section 2. Experimental results are presented in Section 3. The first subsection of Section 4 develops the heat equations used for the thermal analysis of homogeneous stages. Then full-field experimental data using thermography and digital image correlation are examined throughout the deformation process in order to analyse the deformation mechanisms involved.

2. Material and experimental procedure

The tested SMA was commercial polycrystalline Ti–50.8 at.% Ni in the form of a thin tube with an external diameter of 6 mm and a wall thickness of 0.12 mm. The tube was produced by Minitubes SA Company (Grenoble, France). The manufacturing route, and more precisely the final cold-drawing followed by ageing at approximately 773 K for 15 min, gave the tube its final superelastic properties at human body temperature and grain sizes smaller than 10 μm.

A specimen for differential scanning calorimetry (DSC) was cut from the tube using a low-speed diamond cut-off wheel as a thin annular strip of 1.3 mm in width and 5 mm in length. DSC measurements are shown in Fig. 2. On cooling, the transformation from austenite phase (A) to the rhombohedral phase (R) begins at approximately $R_s = 291$ K with a peak at 285 K. It is completed at 275 K. With further cooling, the transformation from the R phase to the martensitic phase (M) begins at 233 K with a peak at 220 K. Upon heating, both transformations are present, but the temperature ranges for the reverse transformation of the R-phase and M-phase overlap. The peak for the $M \rightarrow R$ transformation occurs at 286.4 K, and the reverse transformations are completed at $A_f \approx 299$ K.

The tensile tests were performed on a piece of the tube of 100 mm in length. The sample was fixed in a specially designed gripping system and mounted on a standard ten-
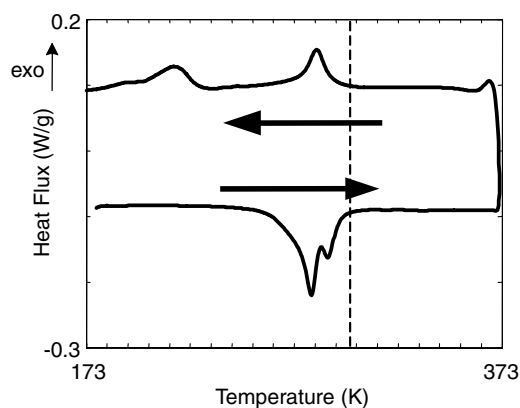

Fig. 2. Differential scanning calorimetry measurements. The dashed line indicates the initial temperature of the tube equal to the room temperature $T_0 = 297$ K.

sile testing machine (Instron 5569, 50 kN). The gauge length of the sample was $L_0 \approx 82$ mm. The gripping system (schematized in Fig. 3(a) and (b)) was created using, at each extremity of the tube, a clamping block comprising two half-cylinders (2), one pin (3) inserted inside the tube (1) to avoid crushing the tube and two final parts (4). Each clamping block (2), (3), (4) is fixed to each of the two extremities of the tube by tightening the two half-cylinders (2) using two screws. Each clamping block is connected to one of the two loading grips of the testing machine through two connectors (6) and (7), which are linked to parts (4) via two sets of self-aligning washers (5). These washers are used to minimize bending and torsion moments that might be induced in the tube (1) during its deformation.

Before being clamped, the tube was heated up to 373 K, 75 K above A_f, and cooled down to room temperature $T_0 = 297$ K (see the dashed line in Fig. 2), just above R_s. Thus, the initial microstructure of the sample was entirely austenitic. Tensile tests were conducted in air at constant cross-head velocity $\dot{U}$.

During tests, the axial force F and cross-head displacement U, as well as the temperature and displacement fields on the outer surface of the tube, were acquired. The thermal and kinematical fields were measured in a observation section of length l_0 shorter than L_0, since the gripping system prohibited observation of upper and lower parts of the gauge section, as illustrated in Fig. 3(a) and (c).

The temperature field T was obtained with a fast multi-detector infrared camera (CEDIP Jade III MW, 145 Hz), with a resolution of 320×240 pixels. The spatial resolution (pixel size), which depends on the adjustment of the focal distance, was estimated to be close to 0.25×0.25 mm^2 for the tests. The surface of the tube was coated with highly emissive black paint in order to obtain black-body properties compatible with the calibration of the camera under the same conditions, which resulted in an accuracy of temperature variations $\theta = T - T_0$ of <0.1 K.

The displacement field **u** was obtained using a visible-light digital camera (Hamamatsu, 1280×1024 pixels, 9 Hz, ambient lighting) and Digital Image Correlation "7D" processing software [11]. The observed outer surface of the tube was covered with a random pattern of white paint speckles, as shown in Fig. 3(c) and (d). Strain fields are calculated from the displacement fields **u**. The elementary cell of the correlation grid was 10×10 pixels so that the spatial resolution was estimated to be of the order of 0.5×0.5 mm^2, as shown in Fig. 3(d). With such parameters, the accuracy on the strain measurement was <0.1%.
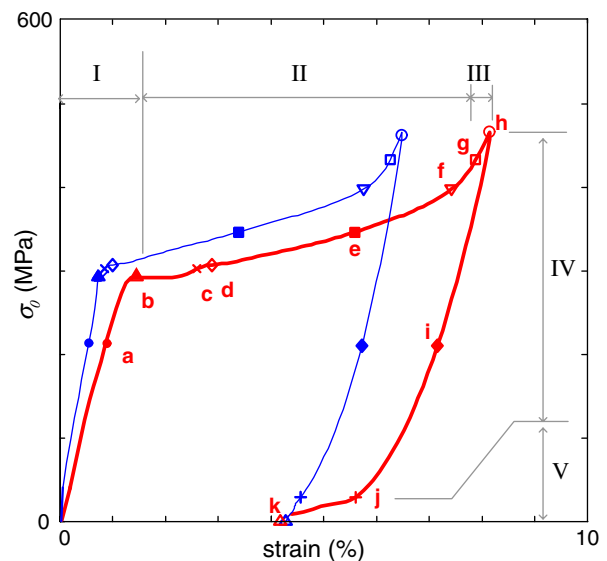

Fig. 4. Nominal stress σ_0 vs. global axial strain ε_{L0} (thick curve) and average axial strain ε_{l0} (thin curve). ε_{L0} is determined from the cross-head displacement U and the sample gauge length L_0. ε_{l0} is determined from the optical measurements of the displacements of the two points A and B in Fig. 3(c). Markers and letters a–k indicate selected times in Figs. 5–12.
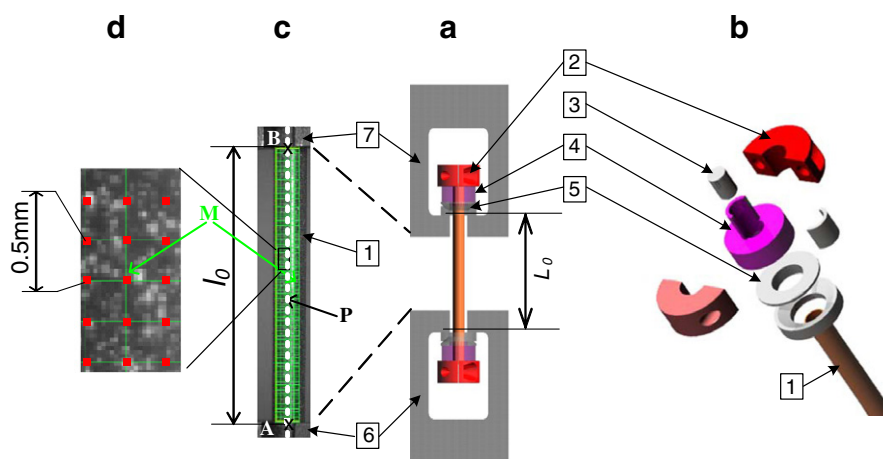

Fig. 3. Scheme of the experimental set-up. (a) Tube specimen with the gripping system. (b) Detail of the fixation of the upper tube extremity with one gripping set linked to the connector (7) by self-aligning washers (5). (c) Image of the observation section with the virtual grid used to compute the kinematics field. (d) Close-up showing the virtual grid and the surface of the tube coated with a random pattern of white painted speckles superimposed on black paint.
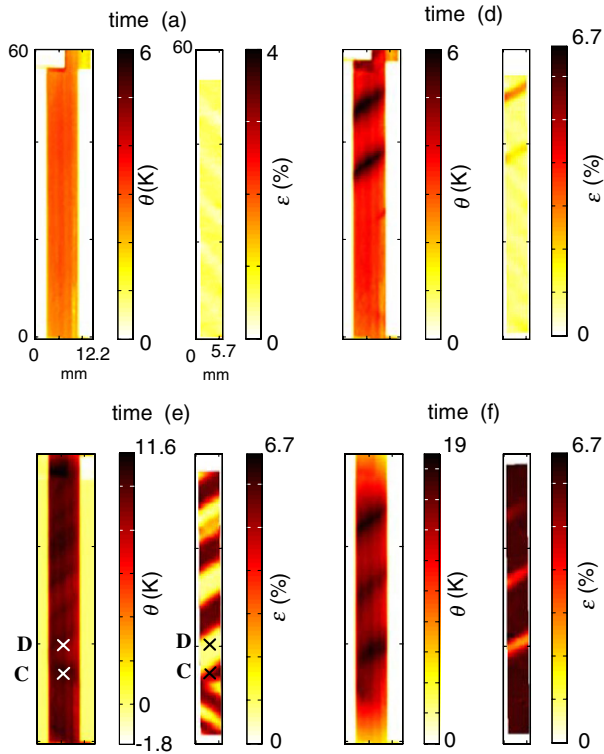
Fig. 5. Coloured maps showing the temperature variation $\theta(M)$ (left) and the local strain $\varepsilon(M)$ (right) fields on the surface of the deformed tube at four selected times marked in Fig. 4.
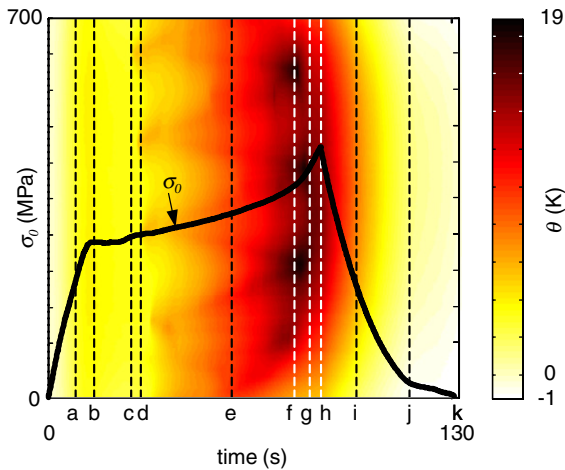

Fig. 6. Coloured map showing the time evolution of $\theta(P)$ at the spatial points P located on the vertical dashed line plotted in Fig. 3(c). Superimposed curve: time evolution of the engineering stress $\sigma_{0.}$.

Figs. 4–12 present results obtained on one tube deformed under tension in air at a cross-head velocity $\dot{U} = 0.08$ mm s^{-1}, i.e., at a global nominal axial strain rate $\dot{U}/L_0 \approx 10^{-3}$ s^{-1}. In this paper, the deformation is characterized by one axial scalar strain defined by $\varepsilon_{X0} = \ln(X/X_0)$, where X_0 is the initial length of one segment initially aligned with the tension axis, whereas X is its length after deformation. Taking $X_0 = L_0$ leads to a global strain ε_{L0} obtained by approximating the current gauge length L by
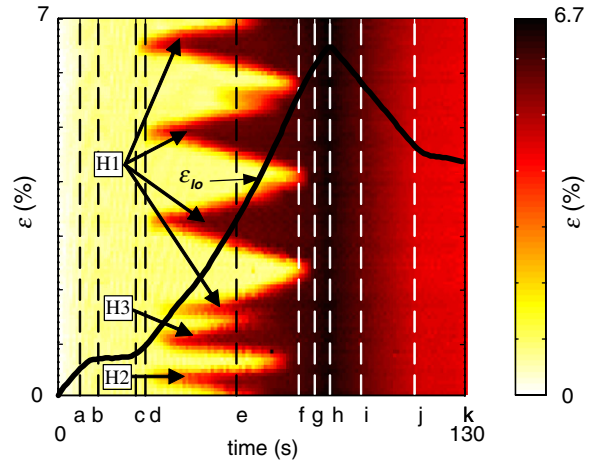
Fig. 7. Coloured map showing the time evolution of $\varepsilon(P)$ at the spatial points P located on the vertical dashed line plotted in Fig. 3(c). Superimposed curve: time evolution of the average axial strain ε_{l0}.

Fig. 8. Time histories of the engineering stress σ_0 and of the temperature variations θ at two spatial points C and D shown in Fig. 5 for the time (e).

Fig. 9. Time histories of the average axial strain ε_{l0} and of local strains $\varepsilon(C)$ and $\varepsilon(D)$ at two spatial points C and D shown in Fig. 5 for the time (e).
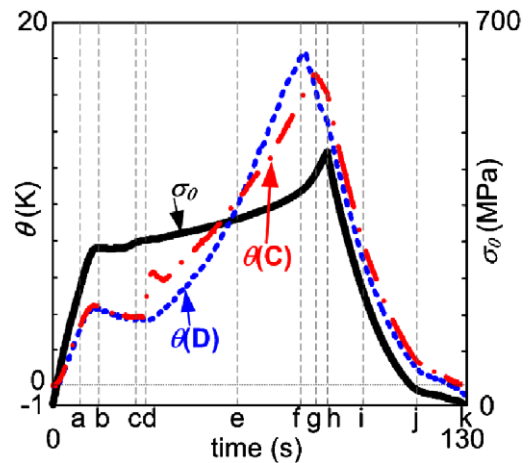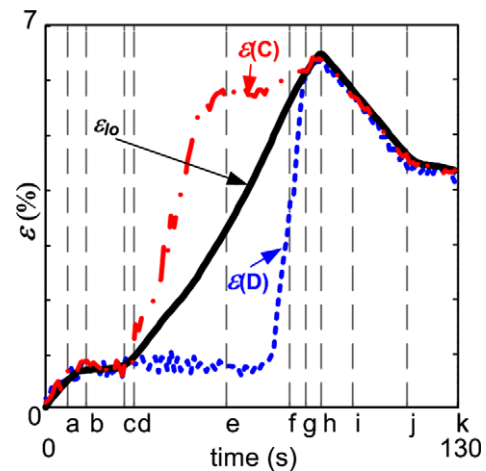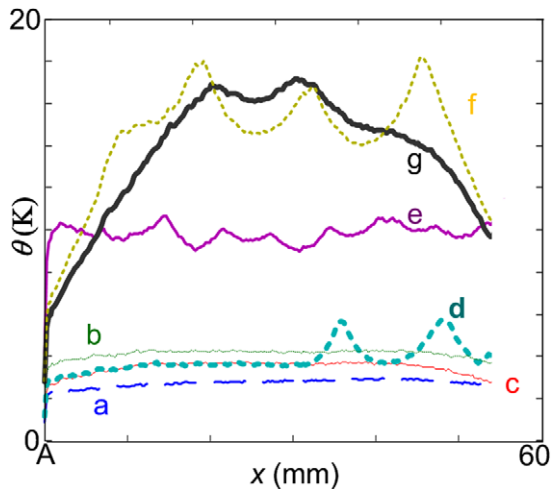
Fig. 10. Profiles $\theta(P)$ showing the temperature variations for the spatial points P located on the vertical dashed line plotted in Fig. 3(c) at selected times a–g marked in Fig. 4.
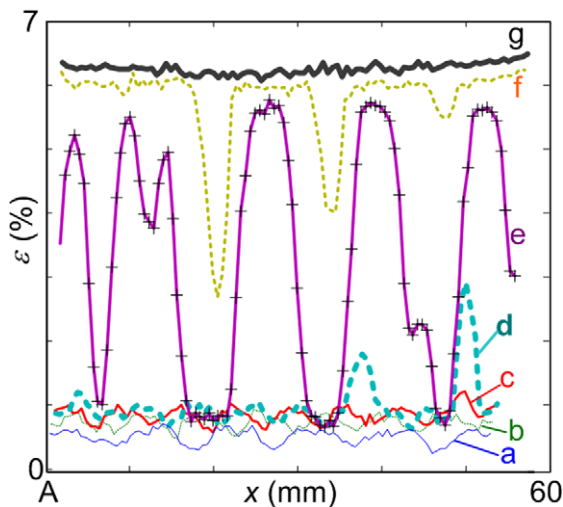

Fig. 11. Profiles $\varepsilon(P)$ showing the strains for the spatial points P located on the vertical dashed line plotted in Fig. 3(c) at selected times b–g marked in Fig. 4.
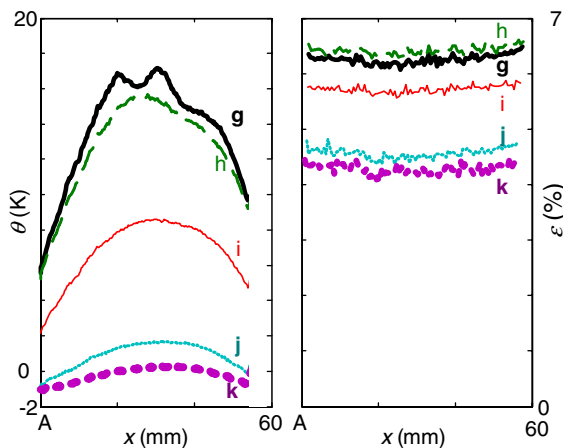

Fig. 12. Profiles $\theta(P)$ (left) and $\varepsilon(P)$ (right) of the temperature variations and strains, respectively, for the spatial points P located on the vertical dashed line plotted in Fig. 3(c), at selected times g–k marked in Fig. 4.

$L_0 + U$. Taking $X_0 = l_0$ leads to an average strain ε_{l0} in the observation section. The current length l is deduced from measurements obtained with the visible-light camera which allow the displacements of the two extremities A and B of the dashed line plotted in Fig. 3(c) to be calculated. Lastly, kinematic field measurements allow one to determine local axial strains $\varepsilon(M)$ from the displacement differences of two vertically aligned points initially dl_0 apart and located around the point M of the observation section (Fig. 3(c) and (d)). A gauge length dl_0 of 10 pixels, corresponding to ~0.5 mm, will be used in the following.

3. Results

The curves plotted in Fig. 4 show the nominal axial stress $\sigma_0 = F/S_0$ (S_0 being the initial cross-section of the tube) as a function of the global strain ε_{L0} (thick curve) and of the average axial strain ε_{l0} (thin curve). The observed engineering stress–strain behaviour (thick curve) is typical of polycrystalline Ni–Ti SMAs with initial austenite phase microstructures. Such engineering stress–strain curves are usually divided into several more or less distinct regions [8].

Stage I (0–a–b): This initial almost linear part of the stress–strain curve is conventionally attributed to the elastic deformation of the austenite phase.

Stage II (b–g): Starts with a slight overshoot followed by a small horizontal stress plateau (b–c) visible until a strain ε_{L0} of approximately 2.5%. Then, the nominal stress increases smoothly (c–g) and subsequently more abruptly in stage III (g–h). It is conventionally postulated that at point (b), the stress reaches a critical value for which the stress-induced martensitic transformation starts [2]. Stage II is conventionally considered to be associated with nucleation and propagation of heterogeneous macroscopic transformation–deformation bands, the increasing slope being due to thermal effects [3,8]. Transformation is assumed to be complete at point (g).

Stage III (g–h): Is conventionally seen as the elastic deformation and further detwinning of the M phase.

Stage IV (h–j): These two last phenomena are considered as the main deformation processes during the first part of the unloading curve.

Stage V (j–k): Reverse transformations are postulated to start only at point (j). As the testing temperature was of the order of A_f, note that the reverse transformation was not completed at the end of the unloading.

Almost the same stages are observed in the σ_0–ε_{l0} thin curve of Fig. 4. The differences between σ_0–ε_{L0} and σ_0–ε_{l0} curves are clearly very dependent on the deformation range. In the sub-stage (0–a) of stage I, ε_{L0} and ε_{l0} vary almost proportionately. In (a) ($\sigma = 200$ MPa) ε_{L0} and ε_{l0}

are equal to 0.9% and 0.53%, respectively. During the sub-stage (a–b), the difference between ε_{L0} and ε_{l0} keeps growing, with ε_{L0} and ε_{l0} increasing by 0.63% and 0.22%, respectively. This difference increases drastically during the horizontal plateau (b–c) of stage II, leading to respective values for ε_{L0} and ε_{l0} of 2.85% and 0.85% in (c). During part (d–g) of stage II, ε_{l0} and ε_{L0} both increase by 5.5%. During stages III and IV, ε_{L0} and ε_{l0} evolve almost proportionately, whereas the decrease in ε_{L0} is much higher than that of ε_{l0} during the last stage V.

Fig. 5 shows coloured maps of the local temperature variation $\theta(M)$ and local strain $\varepsilon(M)$ fields on the surface of the tube at four selected times (a), (d), (e) and (f) marked in Fig. 4. Coloured spatiotemporal maps displayed in Figs. 6 and 7 correspond to time evolutions of $\theta(P)$ and $\varepsilon(P)$ for points P located on the vertical dashed line sketched in Fig. 3(c). The superimposed curve plotted in Fig. 6 represents the time evolution of the nominal stress σ_0. The superimposed curve displayed in Fig. 7 represents the time evolution of the average strain ε_{l0}. Curves plotted in Fig. 8 represent the time histories of σ_0 and of $\theta(C)$ and $\theta(D)$, whereas curves in Fig. 9 represent the time histories of ε_{l0} and of $\varepsilon(C)$ and $\varepsilon(D)$. C and D are two spatial points sketched in Fig. 5(e). They have been taken to be located near the tube extremity which did not move during the test so that $\theta(C)$, $\theta(D)$, $\varepsilon(C)$ and $\varepsilon(D)$ can be considered as temperature variations and local strains for almost constant material points. Figs. 10 and 11 show profiles of $\theta(P)$ and $\varepsilon(P)$ for selected times (a)–(g) defined in Fig. 4. Fig. 12 shows similar temperature variations $\theta(P)$ and strain $\varepsilon(P)$ profiles for selected times (g)–(k) defined in Fig. 4.

Figs. 4–12 lead to the following comments:

Stage I (0–b): During this stage, the deformation of the tube proceeds homogeneously in the observed region, as demonstrated in the snapshot (a) of Fig. 5 and in Figs. 7, 9 and 11. An almost homogeneous temperature increase is observed (Figs. 6, 8 and 10), starting as soon as the tensile deformation proceeds. It is also observed that during the sub-stage (0–a), both stress σ_0 and strain ε but also temperature variation θ increase almost linearly with time (see Figs. 8 and 9 for points C and D). At time (a), for any point of the observed region $\theta \approx 3$ K (Figs. 6, 8 and 10), $\sigma \approx 200$ MPa and $\varepsilon \approx 0.53\% \approx \varepsilon_{l0}$ (Figs. 7, 9 and 11). During the sub-stage (a–b), the time evolutions of σ_0, θ and ε are less and less linear. A temperature decrease is even measured just before time (b). However, at time (b), the temperature variations θ (profile (b) in Fig. 10) and strains ε (profile (b) in Fig. 11) still remain uniform throughout the observed tube length.

Stage II (b–g): During the sub-stage (b–c) of stage II, θ decreases almost homogeneously in the observed region (Figs. 6, 8 and 10) whereas the local strain ε remains homogeneous and almost constant (Figs. 7, 9 and 11). During the sub-stage (c–g), temperature $\theta(M)$ and strain $\varepsilon(M)$ maps (d), (e) and (f) of Fig. 5 reveal a highly heterogeneous deformation of the tube. The time evolutions of θ (Fig. 8) and ε (Fig. 9) for the two points C and D are different and

the profiles sketched in Figs. 10 and 11 for selected times (d)–(f) exhibit very strong gradients. Analysing more precisely both thermal and strain maps (d) of Fig. 5, it is observed that a thin helical band (H1 in Fig. 7) with higher strains ε and temperature variations θ appears from the upper gripping zone and propagates along the observation zone using a helical trajectory inclined at about 58° to the loading axis. Increasing tensile deformation (map (e) of Fig. 5) induces propagation and width enlargement of the first band and simultaneously the appearance of two intertwinning helical bands (H2 and H3 in Fig. 7) originating from the lower gripping zone, with an opposite angle of −58°. The profiles (d) in Figs. 10 and 11 show that at selected time (d) the temperature variation θ and maximal strain ε in the band are, ∼6 K and ∼3%, respectively, whereas they only approach $\varepsilon = 1\%$ and $\theta \approx 3.5$ K in the rest of the sample. Strain profiles (e), (f) and (g) in Fig. 11 demonstrate clearly that the deformation is not homogeneous until the selected time (g) of Fig. 4 even if the slope of the stress–strain curves in Fig. 4 starts to increase between times (f) and (g).

Stage III (g–h): The θ and ε profiles of Fig. 12 show that the temperature is not homogeneous at time (g) in spite of a homogeneous deformation of the tube. This is obviously due to the temperature history during the loading. It is worth noting that the almost homogeneous strain increase between times (g) and (h) is accompanied at any point of the tube by temperature decreases (see also part (g–h) of the curves $\theta(C)$ and $\theta(D)$ in Fig. 8).

Stage IV (h–j): The homogeneous strain decrease (Figs. 7, 9 and 12) is accompanied by a temperature decrease (Figs. 6, 8 and 12), with smooth bell-shaped temperature profiles (Fig. 12). Note that at a given spatial point, the rate of this temperature decrease at the beginning of the unloading stage IV is higher than at the end of the loading stage III (g–h) of the loading, as shown from a comparison of parts (g–h) and (h–i) of curves $\theta(C)$ and $\theta(D)$ in Fig. 8.

Stage V (j–k): Deformation remains homogeneous in the observation region (Figs. 7, 9 and strain profiles (h) and (j) of Fig. 12) and the temperature decrease rate is lower than during stage IV as demonstrated by comparing parts (i–j) and (j–k) of curves $\theta(C)$ and $\theta(D)$ in Fig. 8.

4. Discussion

Although experimental observations of tensile tests on NiTi SMA specimens and of localization phenomena occurring during these tests can be found in the references cited earlier [1–9], simultaneous measurements of temperature and strain fields are unique. They provide new results that enable us to revisit the conventional understanding of the homogeneous and heterogeneous phenomena occurring during tensile tests on NiTi SMAs involving phase transformations.

In order to take advantage of the simultaneous measurements of the strain and temperature fields, some equations are first developed in Section 4.1 below. These equations

will allow us to deduce heat sources from temperature field measurements during stages I and IV and to analyse the deformation mechanisms during these homogeneous stages. When the deformation is heterogeneous, the determination of the heat sources is more difficult and will not been addressed in the present paper [12]. For stages II, III and V, we will focus our analysis on the link between the recorded macroscopic nominal strain–stress tensile curve, the localization topology and the local strain field.

4.1. Hypotheses and basic equations for the analysis of homogeneous stages I and IV

Neglecting any heat source of external origin, heat transfers are governed by the following local heat conduction equation [12–14]:

$$C\dot{T} - \frac{k}{\rho}\text{lap}\,T = \dot{q}, \tag{1}$$

where T and $\dot{T}$ denote the temperature and its rate at any point of the body, respectively. The term "lap T" stands for the Laplacian operator applied to the temperature field. It is assumed that the heat conduction is governed by the standard Fourier's law with an isotropic, uniform and constant thermal conductivity k. The terms ρ and C denote the mass density and specific heat, respectively, which are both assumed to be uniform and constant. $\dot{q}$ is the specific heat source rate (in W kg^{-1}).

For thin specimens like tubes (or sheets), the heat source can be calculated from Eq. (1) and from measurements of temperature fields at the outer surface of the tube; this requires additional assumptions about the temperature distribution in the tube thickness [12]. Eq. (1) can be written in a simpler form when heat sources $\dot{q}$ are homogeneously distributed in a specimen surrounded by ambient medium at temperature T_0 and when specimen temperatures are not too far from the thermal equilibrium [15]. At any point of the outer surface of the tube, this simplified model reads

$$C\left(\frac{\partial\theta}{\partial t} + \frac{\theta}{\tau_{\text{eq}}}\right) = \dot{q}, \tag{2}$$

where $\theta = T - T_0$ is the temperature variation. The parameter τ_{eq} represents a characteristic time reflecting heat losses both by convection through the inner and outer surfaces of the tube and by conduction towards the grip's zones. The above hypotheses used to establish this equation are satisfied during the sub-stage 0–a of stage I and during stage IV.

It is well known that deformation mechanisms for NiTi SMAs include elastic distortion of the atomic lattice and additional mechanisms associated with martensitic and R-phase(s) transformation(s) and variants (de)twinning [16]. Local plastic accommodation of the transformation(s) may also be involved but is effective only for large local strain [7]. The heat source rate $\dot{q}$ involved in Eq. (2) is thus divided into a first rate $\dot{q}_{\text{tr}}$ due to phase(s) transformation(s), a second one $\dot{q}_{\text{thel}}$ due to the usual thermoelastic coupling and finally one $\dot{q}_{\text{diss}}$ due to the intrinsic dissipa-

tions induced by irreversible phenomena, such as plasticity and frictional barriers, opposing interfacial motions:

$$\dot{q} = \dot{q}_{\text{tr}} + \dot{q}_{\text{thel}} + \dot{q}_{\text{diss}} \quad \text{with } \dot{q}_{\text{thel}} = -\frac{\alpha T\dot{\sigma}}{\rho}, \tag{3}$$

where α is the thermal expansion coefficient.

The classical additive decomposition of the strain rate $\dot{\varepsilon}$ is assumed:

$$\dot{\varepsilon} = \dot{\varepsilon}_{\text{el}} + \dot{\varepsilon}_{\text{in}} \quad \text{with } \dot{\varepsilon}_{\text{el}} = \frac{\dot{\sigma}}{E}, \tag{4}$$

where $\dot{\varepsilon}_{\text{el}}$ and $\dot{\varepsilon}_{\text{in}}$ are the elastic and inelastic strain rates, respectively. The inelastic strain rate includes the rate due to transformation(s) $\dot{\varepsilon}_{\text{tr}}$ and the rate due to variants (de)twinning $\dot{\varepsilon}_{\text{de}}$. In the present analysis, the rate due to plasticity is neglected.

Lastly, for any phase transformation, both strain rate $\dot{\varepsilon}_{\text{tr}}$ and heat source rate $\dot{q}_{\text{tr}}$ will be assumed proportional to the transformation fraction rate $\dot{f}$ [14,17]:

$$\dot{\varepsilon}_{\text{tr}} = \dot{f}\varepsilon_{\text{tr}} \quad \text{and} \quad \dot{q}_{\text{tr}} = \dot{f}\Delta H_{\text{tr}}, \tag{5}$$

where ε_{tr} and ΔH_{tr} stand for the transformation strain and specific enthalpy for a complete transformation ($f = 1$).

4.2. Deformation mechanisms in each of the five stages

In the following, we consider and discuss successively the five stages described in Section 3.

4.2.1. Stage I

This stage is conventionally attributed to the elastic distortion of the austenite lattice [2] or of the R-phase lattice [8]. From the thick and thin curves plotted in Fig. 4, two values of the apparent modulus of elasticity are determined as 25 and 40 GPa, respectively. The first (and lower) value is calculated from the nominal strain ε_{L0}. It is deduced from the cross-head displacement which includes the overall tube length variation, but also the elastic deformation of the gripping system and possible sliding of the tube in the gripping system. The second value excludes these experimental errors since the average strain ε_{l0} is calculated from optical measurement of displacements in the observation zone l_0.

There are many references in the literature concerning the values of the apparent modulus of elasticity of NiTi alloys determined from tensile stress–strain tests, both in austenitic and martensitic state [18]. The reported values range from 20 to 50 GPa for martensite and from 40 to 90 GPa for austenite. Our determined value of 40 GPa appears in the lower range of the values reported in the literature for austenite.

By recourse to in situ neutron diffraction during loading, Rajagopalan et al. [19] obtained a modulus as high as 110 GPa, which is representative of the elastic distortion of the atomistic lattice. As already underlined by Liu and Xiang [18] and by Sittner et al. [16], weak values of apparent moduli of elasticity determined from mechanical

stress–strain, as in this work, either in the austenitic or martensitic state, are indications of occurrence of deformation mechanisms other than pure elastic distortion of crystalline lattice.

Indeed, the observed homogeneous temperature increase starting for very low stress during the sub-stage (0–a) suggests an additional deformation mechanism involving an exothermic phase transformation. A pure elastic deformation would have led to a homogeneous temperature decrease associated with the well-known thermoelastic coupling [13], as revealed by Eq. (3) which leads to $\dot{q}_{thel} < 0$ when $\dot{\sigma} > 0$.

The equations developed in Section 4.1 are now used in order to further analyse the sub-stage (0–a) of stage I. With regard to the DSC measurement shown in Fig. 2, the material is initially in the austenitic state. Hence, it will be assumed that during the sub-stage (0–a), the only inelastic mechanism is due to phase transformation(s), i.e., variant (de)twinning and plasticity are neglected, so that $\dot{q}_{diss} \approx 0$. Combining Eqs. (3)–(5) results in

$$\frac{\Delta H_{tr}}{\varepsilon_{tr}} = \frac{\dot{q} + \frac{\alpha T}{\rho}\dot{\sigma}}{\dot{\varepsilon} - \frac{\dot{\sigma}}{E}}. \qquad (6)$$

With regard to the homogeneity of strains and temperature variations during the sub-stage (0–a), heat sources are assumed to be homogeneously distributed throughout the specimen; the heat source rates $\dot{q}$ can thus be estimated from Eq. (2). In this equation, the term θ/τ_{eq} vanishes at the beginning of the sub-stage (0–a), and is likely to remain weak throughout the sub-stage (0–a). In order to confirm this second hypothesis, a second tensile test has been performed at a cross-head velocity 10 times greater than the first test. Temporal evolutions of average strain ε_{l0} are plotted in Fig. 13(a), the one for the first test being plotted using thin lines and a time range of 8 s, whereas that of the second test is plotted using thick lines and a time range of 0.8 s. The stress σ_0 and temperature variation θ evolutions are plotted as functions of average strain ε_{l0} during the sub-stages (0–a) for the first (thin curves) and second

(thick curves) tests in Fig. 13(b) and (c), respectively. The very similar strain–stress (Fig. 13(b)) and strain–temperature (Fig. 13(c)) curves for the two tests lead us to conclude that testing conditions were very close to adiabatic during sub-stage (0–a) in both cases. These almost adiabatic conditions, together with homogeneity of the heat source rate, explain the flat shapes of the θ profiles for selected times (a) and (b) in Fig. 10.

Consequently, based on the previous assumption, Eqs. (2) and (6) show that the transformations involved during the sub-stages (0–a) of the two tests satisfy at any time:

$$\frac{\Delta H_{tr}}{\varepsilon_{tr}} = \frac{C\dot{T} + \frac{\alpha T}{\rho}\dot{\sigma}}{\dot{\varepsilon} - \frac{\dot{\sigma}}{E}}. \qquad (7)$$

Two types of transformation can be observed starting from an austenite phase, i.e., either A–R or A–M transformation. A third transformation R–M can occur from the R-phase. Transformation strain ε_{tr} for a complete A–R transformation is of the order of 1% [20], that for a complete A–M transformation of the order of 8%, and that for a complete R–M transformation of the order of 7% [21]. The enthalpy changes ΔH_{A-R}, ΔH_{A-M} and ΔH_{R-M} associated with these three transformations are of the order of 6, 20 and 14 J g^{-1}, respectively [22]. This leads to

$$\frac{\Delta H_{tr}}{\varepsilon_{tr}} = 600 \text{ J/g} \quad \text{for } A\text{–}R,$$

$$\frac{\Delta H_{tr}}{\varepsilon_{tr}} = 250 \text{ J/g} \quad \textit{for } A\text{–}M \quad \text{and}$$

$$\frac{\Delta H_{tr}}{\varepsilon_{tr}} = 200 \text{ J/g} \quad \text{for } R\text{–}M. \qquad (8)$$

Comparison of the experimentally determined values $\frac{\Delta H_{tr}}{\varepsilon_{tr}}$ using Eq. (7) with the above three values for the A–R, and A–M and R–M transformations will allow us to deduce which transformation(s) occur(s) during the sub-stage (0–a). In the following, the value $E = 110$ GPa determined by neutron diffraction [19] will be considered as the true elastic modulus for austenitic, martensitic and R-phase. The specific heat will be considered as constant, uniform and equal to $C = 0.49$ J K^{-1} g^{-1} [23].
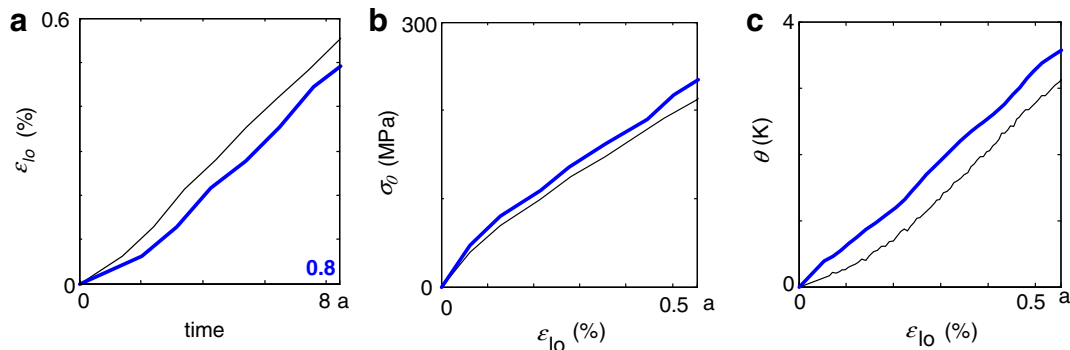

Fig. 13. (a) Average strain ε_{l0} as function of time during sub-stage 0–a for the test shown in Fig. 4 (thin curve, time range 0–8 s) and for a second test performed with a cross-head velocity 10 times higher (thick curve, time range 0–0.8 s). (b) Stress σ_0 as function of average strain ε_{l0} for these two tests. (c) Temperature increase θ is function of average strain ε_{l0} for these two tests.
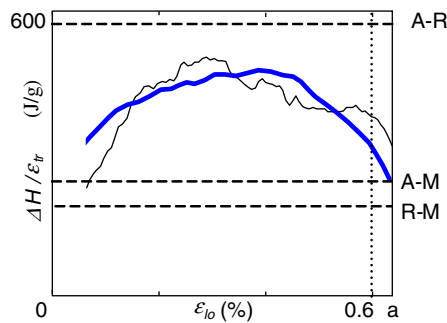
Fig. 14. Ratio of the transformation specific enthalpy to the transformation strain, $\Delta H_{tr}/\varepsilon_{tr}$, as function of average strain ε_{l0} during the sub-stage 0–a. The two plain curves are calculated from Eq. (7) and from the experimental results shown in Fig. 13, for the test shown in Fig. 4 (thin curve) and for a second test 10 times faster (thick curve). The three horizontal dashed lines represent the value of ($\Delta H_{tr}/\varepsilon_{tr}$) for complete A–R, A–M and R–M transformations.

The measured ratios $\Delta H_{tr}/\varepsilon_{tr}$ along the sub-stage (0–a) are plotted as function of the strain in Fig. 14, for the two tests performed at moderate and high strain rates using thin and thick lines, respectively. The upper, medium and lower dashed horizontal straight lines are the three values calculated for the A–R, A–M and R–M transformations, respectively. These two curves $\Delta H_{tr}/\varepsilon_{tr}$ demonstrate that the deformation during the sub-stage (0–a) is never purely elastic. For very low stress and strain levels the deformation involves additional mechanisms associated with a mixture of the three types of transformation (A–R, A–M and R–M). This result agrees with two observations already reported in the literature. First, A–R transformation is known to proceed for specific NiTi SMAs throughout the whole part of the tensile stress–strain curve preceding the stress peak [16,20]; the stress–strain curves associated with this transformation are reported to be linear or not and can present very short stress plateaux. Second, macroscopically homogeneous and stable A–M transformation, referred as "pre-burst transformation" or "incubation" [7,24], can be involved in this stage. Our result is not surprising but is still qualitative. It is based on strong assumptions, as evident in Eqs. (2) and (3), and on values for physical parameters (E, ε_{A-R}, ε_{A-M}, ε_{R-M}, ΔH_{A-R}, ΔH_{A-M} and ΔH_{R-M}) that are difficult to determine. Qualitatively, the proportion of each transformation is not constant throughout the homogeneous loading stage and it is not possible to distinguish during this stage a period during which only A–R transformation occurs.

4.2.2. Stage II

In quasi-isothermal conditions, this stage is associated with a localized Lüders-like deformation over a stress plateau through the motion of localized bands. The measured engineering stress σ_0-average strain ε_{l0} curve shown in Fig. 4 does not exhibit a stress plateau; however, it has been shown that despite the positive slope of the stress–strain curve, deformation proceeds heterogeneously. It is conventionally regarded that the beginning and the end

of this plateau are associated with the beginning and the end of the stress-induced transformation [2]. The analysis of the thermal, kinematical and mechanical measurement during the stage I has proved that the A–R, A–M and R–M transformations start before the onset of localization.

The positive slope can be tentatively analysed from our thermal measurements. The well-known Clausius–Clapeyron relation [25] expresses the transformation stress as a linear function of temperature; it is worth recalling that the Clausius–Clapeyron relation is valid locally where the transformation occurs and that the linear coefficient depends on the stress state, e.g., it is different in tension, compression and shear for a given alloy [5]. When the temperature of the specimen is heterogeneous, the application of the Clausius–Clapeyron relation would require knowledge of which spatial point of the tube the transformation occurs at, and of the local stress state at this point. It is thus difficult to analyse in detail the engineering stress–strain slope at each position of the heterogeneous stage II. Nonetheless, times (c) and (e) are simpler to analyse since the temperature is almost homogeneous for these two times, as shown by profiles (c) and (e) in Fig. 10. The temperature increase from (c) to (e) is equal to 7 K, whereas the stress increase is of the order of 40 MPa. If we assume that the positive slope is only due to temperature increase, a coefficient of 40/7 = 5.7 MPa K^{-1} is obtained for the Clausius–Clapeyron relation, which is in the range of the values reported in the literature for tensile experiments [26].

The macroscopic deformation patterns observed in our test are helical bands initiating in the grip zones. It is known that band formation, morphology and propagation depend on a number of factors, including specimen shape, loading rate, heat transfer conditions, gripping system, heat treatment conditions, etc. [1–5]. In our tests, the helical bands propagate (domain lengthening) and widen (domain lateral thickening) with deformation, maintaining their helical shape throughout the whole test.

Experiments on NiTi tubes are less common than on wires or strips [1–5]. The few published papers on tubes [6,8,24] have reported experimental results on macroscopic deformation instability and domain morphology in superelastic and ferroelastic NiTi SMA microtubes. In Ng and Sun's experiments [8], the band shape has been observed changing from an inclined cylinder to helical shape with increasing testing temperatures [8], the transition temperature being a few degrees above A_f. For a testing temperature well above this transition temperature, Feng and Sun [24] have observed initiation of localization through helical bands which subsequently evolve in a complex way between various domain morphologies during loading and unloading. They explain these domain pattern evolutions by competition between macroscopic domain wall energy (interfacial or front energy) and bulk strain energy of the overall tube. The differences in total energy (bulk strain energy and interfacial domain energy) among all the possible states of domains in the tube system lead to morphology transitions. The interfacial energy is depen-

dent on the forms of the domains, e.g., helical domain or ring-like domain. The bulk strain energy is highly influenced by the interaction between material and structure geometry.

The present test temperature is of the order of A_f. The initiation of the localization through helical bands agrees thus with Ng and Sun's results [8]. However, we did not observe any evolution of the domain morphology during the heterogeneous deformation stage. This effect is apparently in contradiction with Feng and Sun's experiments [24]. Two factors influencing the bulk energy of the overall tube have to be noted here. The first factor is the smaller thickness/mean radius ratio (here of the order of 0.04) compared to the cases of microtubes tested by Sun et al. ranging from 0.2 [6,24] to 0.5 [8]. This factor reduces the strain, stress and temperature heterogeneities in the tube thickness, thus diminishing the shell effects of the tube wall, which behaves rather like a membrane. The second factor is the design of the gripping system and especially the use of self-aligning washers which allows the two extremities of the specimen to rotate with weak resistive torques. The specimen is submitted only to tensile load and is free to deform asymmetrically through the development of helical bands. This is not the case for the gripping system used in [24] which transmits bending moment and torque to the tubular specimen as soon as the deformation of the tube is no longer axisymmetric, thereby strongly influencing the observed phenomena of morphology evolution. It is worth concluding that comparisons of our experimental results with those of Sun et al. [6,8,24] highlight the strong influence of the structure–material coupling on the evolution of domain morphology.

Results obtained in this work also give some valuable information on the evolution of the heterogeneous strain field during the stress "plateau". For instance, the initiation of the bands at the extremities of the gauge section L_0 easily explains the large difference between increases of ε_{L0} and ε_{l0} during the sub-stage (b–c) of stage II. During this sub-stage, local strains $\varepsilon(M)$ inside the observation region remain constant (a small decrease is even measured), and the temperature decrease is due to heat exchange with the surroundings. This heat exchange occurs both through outer and inner surfaces of the tube by convection and by conduction mainly along the axis of tube. The temperature decrease between profiles (b) and (c) in Fig. 10 is mainly due to heat loss by convection, whereas heat loss by conduction toward the cooler grips explains the slightly increasing bell-shape.

Furthermore, during the sub-stage (c–f) of stage II, the deformation proceeds through localized deformation bands (LDBs), here helical bands, separated from the less-deformed regions by narrow regions, called hereafter band boundaries (BBs), across which strains and temperatures change very rapidly. Analysing temperature fields in order to extract meaningful local heat sources occurring during this heterogeneous stage is not straightforward; it requires the development of a temperature data processing system, which is in progress [12].

In this paper, we will consequently restrict our analysis during the sub-stage (d–g) to the observation of the strain fields. The first result concerns the strain evolution between the different regions of the heterogeneously deformed tube. It is worth recalling that in the present experiments, the "local" strain $\varepsilon(M)$ was calculated with a gauge length of 0.5 mm, as indicated by the crosses plotted in the profile (e) in Fig. 11. Temporal evolutions of $\varepsilon(C)$ and $\varepsilon(D)$ in Fig. 9 show that when the BB of an LDB passes a certain point, there is a sudden increase of the local strain rate. This local strain rate keeps finite and the local strain at one point (e.g., $\varepsilon(C)$) continues to increase after the BB has passed. The continuous time evolution of the local strain at one material point is illustrated in Fig. 15 for the first band initiating in the upper grip. In this figure, the strain is plotted as function of the initial coordinates x_0 (whereas spatial coordinates were used in Figs. 10–12 for θ and ε) for all points P in Fig. 3(c) of initial coordinates greater than 44 mm. These profiles are plotted for the selected times (c), (d), (e), (f), (g) and (h) and for four times between (d) and (e) shifted by 5 s. Crosses on these profiles indicate the points P at a distance of 0.5 mm where "local" strains are measured.

Strain profiles along a LDB shown in Fig. 15 demonstrate that the bands nucleate neither with their final width nor with a strain level equal to the peak strain. In fact a narrow band (profile (d)) is nucleated which expands in its width direction with increasing peak strain level (evolution (d), (e)). Once the BB has passed a point (evolution between (e) and (f)), the strain continues to increase. This is probably due to an incomplete transformation inside the LDB, as already shown by Brinson et al. [7], Tan et al. [27] and Schmahl et al. [28] using optical microscopy, DSC and X-ray diffraction, respectively.
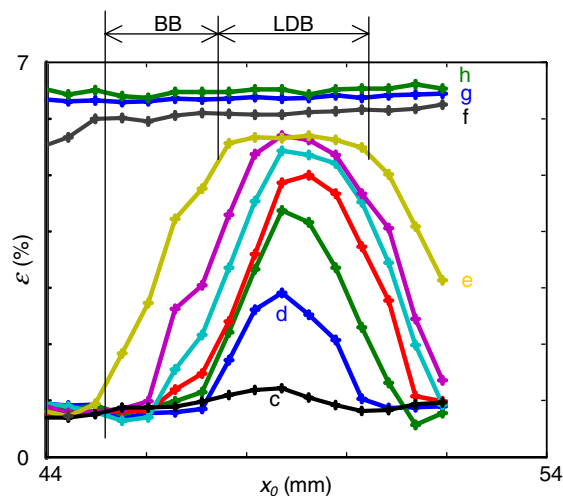

Fig. 15. Profiles of the local strain $\varepsilon(P)$ as function of the initial coordinates for the band initiating in the upper grip region. The profiles are plotted at selected times shown in Fig. 4 and every 5 s between times (d) and (e). LDB and BB designate the localized deformation band and the band boundaries, respectively. They are plotted for the time (e).

For all profiles between (d) and (e) of Fig. 15, the strain gradients in the two BBs on both sides of the LDB are almost independent of the coordinate x_0 and equal to $d\varepsilon/dx_0 = 2.5\%\,\mathrm{mm}^{-1}$. The resulting BB widths at time (e) are of the order of 2 mm, giving a BB width/tube thickness ratio of the order of $2/0.12 = 15$. Such a ratio has to be compared with a ratio of only 1 in Feng and Sun's experiments [24] and also with similar ratios measured for Portevin–Le Châtelier deformation bands which range from 1 to 2 independently of the tensile strain rates [29,30]. The higher value of the present ratio is likely to be induced by strong local thermomechanical coupling at the vicinity of the transforming region, as depicted by the temperature profiles for snapshots (d) to (f) in Fig. 10. This stronger coupling is in turn induced by higher nominal strain rate in our tensile experiment compared to those achieved in [24] (10^{-3} vs. $10^{-5}\,\mathrm{s}^{-1}$) under similar heat exchange conditions. The influence of this coupling has to be further studied in order to introduce essential elements into the theoretical modelling of localization in superelastic behaviour of NiTi SMAs.

4.2.3. Stage III

This stage is conventionally seen as the elastic deformation and further detwinning of the oriented M-phase. During this stage, the temperature profiles shown in Fig. 12 evolve from a wavy, bell-shaped curve (profile (g)) to a smoother bell-shaped curve (profile (h)), whereas the evolution of strain profiles demonstrates homogeneous strain increases. This evolution may be due to homogenous or zero heat sources throughout the tube and to conduction along the length of the tube toward the grips. However, it is not simple to estimate heat source values from the evolution of profiles during this stage, due to the complexity of the thermal process leading from wavy profiles like (g) to smoother ones like (h). No conclusions can be drawn from the full-field measurements during this stage as long as local heat sources are not determined [12].

4.2.4. Stage IV

This stage is conventionally attributed to elastic deformation and detwinning of the oriented M variants formed during loading. However, observation of the time histories of $\theta(C)$ or $\theta(D)$ in Fig. 8 from (g) to (i) indicates that the temperature decrease rate is higher during the sub-stage (h–i) than during stage III (g–h). This proves that the difference in heat source rate between (g–h) and (h–i) is being due to an exothermic heat source during stage III and/or an endothermic heat source starting at the beginning of the unloading. The aim of the next paragraph is to verify the existence of this hypothetical endothermic heat source and to analyse more in detail the physical mechanisms involved during unloading (stage IV).

For that purpose, a third test has been performed. The tube was first heated to 373 K and cooled down to room temperature; it was then deformed in tension loading under the same conditions as those of the first test, but the defor-

mation was stopped at the end of the loading by holding the specimen at constant displacement for 35 s. It is assumed that negligible transformation occurs during the rest time noted ($h^- h^+$). The natural temperature decrease θ_{nd} was then recorded (part $h^- h^+$ in Fig. 16(a)). The two plain thick and thin curves in Fig. 16(a) represent time evolutions of temperature variations of two points of the tube sketched in Fig. 16(b). The modelling of this natural decrease using Eq. (2) requires the identification of a characteristic time τ_{eq}. The two dashed curves plotted in Fig. 16(a) show that the natural decrease is well modelled using Eq. (2) with $\dot{q} = 0$ and $\tau_{eq} = 22 \pm 1$ s. After a rest of 35 s (point h^+), the unloading was continued, leading immediately to a faster temperature decrease. This faster temperature decrease cannot be explained by thermoelastic coupling, which would reduce temperature decrease for decreasing stress ($\dot{q}_{thel} > 0$ when $\dot{\sigma} < 0$ in Eq. (3)). It is thus obvious that an endothermic heat source occurs as soon as the specimen is unloaded and that three main mechanisms are involved during the unloading, i.e. elasticity, detwinning and reverse transformation, with plasticity being neglected.

Taking into account Eq. (4), the additive decomposition of the strain rate is thus expressed as

$$\dot{\varepsilon} = \dot{\varepsilon}_{el} + \dot{\varepsilon}_{tr} + \dot{\varepsilon}_{de} = \frac{\dot{\sigma}}{E} + \frac{\dot{q}_{tr}}{\Delta H_{tr}}\varepsilon_{tr} + \dot{\varepsilon}_{de}, \qquad (9)$$

where $\dot{\varepsilon}_{de}$ is the detwinning strain rate. During unloading, the value of the endothermic heat source rate can be estimated from Eq. (2) with $\tau_{eq} = 22$ s since the homogeneity of the strain field, as demonstrated by the evolution of profiles (h), (i) and (j) in Fig. 12, suggests a homogeneous transformation strain rate during this stage, associated with homogeneously distributed heat sources inside the tube. The transformation strain rate $\dot{\varepsilon}_{tr}$ can therefore be deduced from Eq. (9), if the two values ΔH_{tr} and ε_{tr} involved during unloading stage IV are known. At the end of loading, the material is at least 70% martensitic [7]. The endothermic phase transformation is thus likely to be mainly
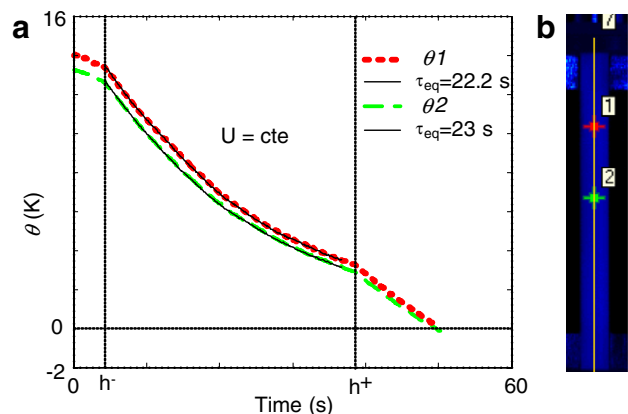

Fig. 16. For a test similar to the test shown in Fig. 4 but stopped at time (h) 35 s ($h^- h^+$) before unloading. The dashed curves represent the time evolutions of the temperature variations θ_1 and θ_2 of the two points 1 and 2 shown in (b). The plain curves show the modelling of these temporal evolutions using Eq. (2), assuming a zero heat source during the rest $h^- h^+$.
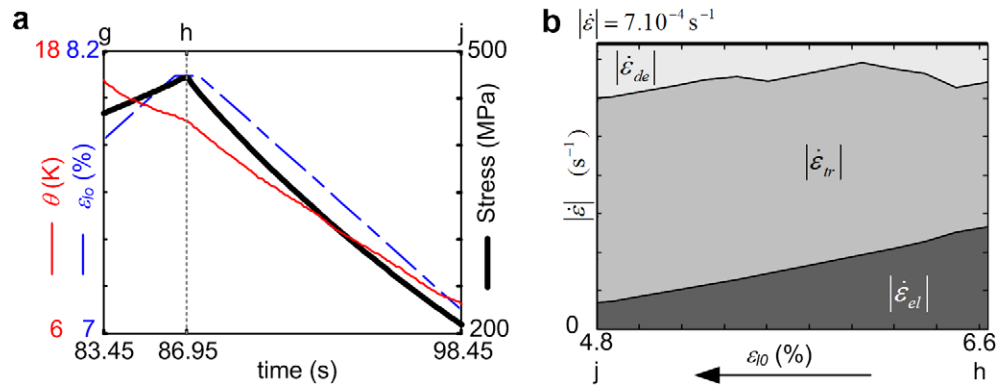
Fig. 17. (a) Stress σ_0 (thick curve), strains ε (dashed curve) and temperature variations θ (thin curve) as functions of time during the sub-stage h–j for the test shown in Fig. 4. (b) Estimation of the elastic, transformation and detwinning strain rates as function of the strain ε_{l0} during the unloading sub-stage h–j.

a M–A transformation, which leads to $\Delta H_{tr} \approx \Delta H_{M-A} = 20 \text{ J g}^{-1}$ and $\varepsilon_{tr} \approx \varepsilon_{M-A} = 8\%$.

Fig. 17(a) shows the stress σ_0, strain ε and temperature variation θ as functions of time during the unloading stage IV. Thus, from these measurements and Eq. (9), the absolute values of the elastic $\dot{\varepsilon}_{el}$, reverse transformation $\dot{\varepsilon}_{tr}$ and detwinning $\dot{\varepsilon}_{de}$ strain rates are plotted in Fig. 17(b) as functions of the strain ε_{l0} between times (h) and (j).

As evident from Fig. 17(b), deformation mechanisms other than pure elastic distortion of crystalline lattice occur as soon as the stress starts to decrease. From the above rough analysis, it is suggested that reverse phase transformation has a predominant effect throughout the unloading. Its contribution to the overall strain rate is almost constant and equal to half the total strain rate. Decreasing the strain ε_{l0} leads to a reduction in the elasticity contribution and to an increase in the detwinning phenomena. It is worth concluding that these results contradict the usual assumption of elastic unloading which is commonly made in thermomechanical modelling for stage IV.

4.2.5. Stage V

This stage appears very similar to the sub-stage (b–c) of loading stage II. Reverse localized bands are likely to form at the extremities of the tube, outside the observation region. This hypothesis would explain the high decrease of the nominal strain ε_{L0} and the almost constant average strain ε_{l0}. As the local strains $\varepsilon(M)$ remain constant in the observation zone, the temperature decreases at a slower rate, as a result of natural heat losses only.

5. Conclusion

The tensile behaviour of an initially austenitic Ti–50.8 at.% Ni thin-walled tube was investigated using synchronized measurements of the temperature and strain fields. The following points are the main results of this study:

1. The apparent initial linear elastic stage during loading is a homogeneous deformation stage, involving a mixture of partial $A \rightarrow R$, $A \rightarrow M$ and $R \rightarrow M$ transformations.

These transformations start as soon as the deformation proceeds as revealed by an immediate temperature increase. This stage does not correspond to pure elastic deformation of the austenitic phase as often assumed in modelling.

2. The previous observation indicates that the stress peak on the stress–strain curves cannot be regarded as being due to the nucleation of the product phase of the corresponding transformations.

3. The stress plateau is only a manifestation of the localization of deformation. The transformations start before this plateau and are incomplete at the end of the plateau. The experimentally measured plateau stress and plateau strain do not correspond to the martensitic transformation stress and strain of NiTi as often assumed in modelling.

4. Localization can occur even if the tensile stress–strain curve does not exhibit a clear peak and plateau. The positive slope is due to the thermal effect.

5. Localization is associated with macroscopic deformation instabilities leading to deformation bands (LDBs) throughout the specimen. The type and evolution of the morphology of these bands are dependent on a number of factors, including specimen gripping technique. In our tests, the gripping system applies negligible bending and rotating torques to the tube extremities and localization occurs through helical bands inclined at about 58° to the loading axis.

6. The LDBs are separated from the low deformation regions by the BBs. The strain gradient inside these BBs is constant, equal to 2.5% mm^{-1}, for the investigated experimental conditions. This value should be highly dependent on thermal effects.

7. The LDBs do not nucleate with their final width and peak strain level, revealing that the transformation is never complete inside these LDBs.

8. During the early stage of unloading, the apparent linear elastic stage is a homogeneous deformation stage, involving detwinning and reverse transformations as soon as the unloading proceeds. Reverse transformation is the main deformation mechanism during unloading,

leading to a transformation strain rate approximately equal to half the total strain rate. The detwinning strain rate is of the same order as the elastic strain rate. This unloading stage does not correspond to pure elastic deformation of oriented martensite as often assumed in modelling.

9. No lower stress plateau was observed in our experiments due to the testing temperature being of the order of A_f. Further studies are in progress to analyse deformation mechanisms during lower stress plateaux. This will be achieved by increasing testing temperature (although measurements of temperature and strain fields are then difficult) or by performing tests at room temperature using alloys with lower A_f temperatures.

The synchronized measurements of both temperature variation and strain fields have thus yielded important information for analysing coupling effects and deformation mechanisms associated with stress-induced transformations in SMAs. However, such an analysis in zones of heterogeneous deformation modes is restricted, mainly due the difficulty of analysing the phase transformation(s) directly from thermal fields. The development of a temperature data processing software [12] is in progress in order to improve our analysis. This software should provide a better estimate of the history of heat source fields from the history of the measured temperature fields, as was done in previous studies [31,32].

A second improvement is planned to permit a finer quantitative analysis. This will be based on the use of higher-magnification lenses for both visible-light and infrared digital cameras in regions crossed by the bands. This will allow a better accuracy on the local strain and heat source fields in the boundaries of localized bands.

Acknowledgement

References

[1] Miyazaki S, Imai T, Otsuka K, Suzuki Y. Scripta Metall 1981;15:853–6.
[2] Shaw JA, Kyriakides S. J Mech Phys Solids 1995;43:1243–81.
[3] Shaw JA, Kyriakides S. Acta Mater 1997;45:683–700.
[4] Favier D, Liu Y, Orgéas L, Rio G. In: Sun QP, editor. Solid mechanics and its applications, vol. 101. New York: Kluwer Academic Publishers; 2001. p. 205–12.
[5] Orgéas L, Favier D. Acta Mater 1998;46:5579–91.
[6] Sun QP, Li ZQ. Int J Solids Struct 2002;39:3797–809.
[7] Brinson LC, Schmidt I, Lammering R. J Mech Phys Solids 2004;52:1549–71.
[8] Ng KL, Sun QP. Mech Mater 2006;38:41–56.
[9] Gadaj SP, Nowacki WK, Pieczyska EA. Infrared Phys Technol 2002;43:151–5.
[10] Liu Y, Liu Y, Van Humbeeck J. Scripta Mater 1998;39:1047–55.
[11] Vacher P, Dumoulin S, Morestin F, Mgil-Touchal S. Proc Instn Mech Engrs, ImechE 1999;213C:811–7.
[12] Schlosser P, Louche H, Favier D, Orgéas L. Strain 2007;43:260–71.
[13] Chrysochoos A, Louche H. Int J Eng Sci 2000;38:1759–88.
[14] McCormick PG, Liu Y, Miyazaki S. Mater Sci Eng A 1993;167:51–6.
[15] Chrysochoos A, Maisonneuve O, Martin G, Caumon H, Chezeaux JC. Nucl Eng Des 1989;114:323–33.
[16] Sittner P, Novak V, Lukas P, Landa M. J Eng Mater Technol, ASME 2006;128:268–78.
[17] Lexcellent C, Vacher P. Arch Mech 1993;451:135–55.
[18] Liu Y, Xiang. J Alloy Compd 1998;270:154–69.
[19] Rajagopalan S, Little AL, Bourke MAM, Vaidyanathan R. Appl Phys Lett 2005;86:081901.
[20] Sittner P, Landa M, Lukas P, Novak V. Mech Mater 2006;38:475–92.
[21] Orgéas L, Favier D. J Phys IV 1995;C8(5):605–10.
[22] Liu Y, McCormick PG. Proc. ICOMAT 92. Monterey, CA; 1992. p. 923.
[23] Faulkner MG, Amalraj JJ, Bhattacharyya A. Smart Mater Struct 2000;9:632–9.
[24] Feng P, Sun QP. J Mech Phys Solids 2006;54:1568–603.
[25] Wollants P, De Bonte M, Roos JR. Z Metallkd 1979:70–113.
[26] McCormick PG, Liu Y. Acta Mater 1994;42:2407–13.
[27] Tan G, Liu Y, Sittner P, Saunders M. Scripta Mater 2004;50:193–8.
[28] Schmahl WW, Khalil-Allafi J, Hasse B, Wagner M, Heckman A. Mater Sci Eng A 2004;378:81–5.
[29] Tong W, Tao H, Zhang N, Hector Jr LG. Scripta Mater 2005;53:87–92.
[30] Zhang Q, Jiang Z, Jiang H, Chen Z, Wu X. Int J Plasticity 2005;21:2150–73.
[31] Louche H, Chrysochoos A. Mater Sci Eng A 2001;307:15–22.
[32] Louche H, Vacher P, Arrieux R. Mater Sci Eng A 2006;404:188–96.